International Journal of Solids and Structures 46 (2009) 2659–2668

Contents lists available at ScienceDirect

International Journal of Solids and Structures

journal homepage: www.elsevier.com/locate/ijsolstr

Nonlinear interface shear fracture of end notched flexure specimens

Zhenyu Ouyang [a], Guoqiang Li [a,b,*]

[a] Department of Mechanical Engineering, Louisiana State University, Baton Rouge, LA 70803, USA
[b] Department of Mechanical Engineering, Southern University, Baton Rouge, LA 70813, USA

ARTICLE INFO

Article history:
Received 26 November 2008
Received in revised form 9 February 2009
Available online 26 February 2009

Keywords:
Cohesive zone model (CZM)
Bonded joint
Interface shear fracture
Mode II
Composites
Analytical solution
Arbitrary nonlinear cohesive laws
ENF

ABSTRACT

The nonlinear analytical solutions of an end notched flexure adhesive joint or fracture test specimen with identical or dissimilar adherends are investigated. In the current study, a cohesive zone model (with arbitrary nonlinear cohesive laws) based analytical solution is obtained for the interface shear fracture of an end notched flexure (ENF) specimen with sufficiently long bond length. It is found that the scatter and inconsistency in calculating Mode II toughness may be significantly reduced by this model. The present work indicates that the Mode II toughness G_{IIc} under pure shear cracking condition is indeed very weakly dependent on the initial crack length. And this conclusion is well supported by the experimental results found in the literature. The parametric studies show that the interface shear strength is the most dominant parameter on the critical load. It is also interesting to note that with very short initial crack length and identical interface shear strength, higher Mode II toughness indeed cannot increase the critical load. Unlike the high insensitivity of critical load to the detailed shape of the cohesive law for Mode I peel fracture, the shape of the cohesive law becomes relatively important for the critical load of joints under pure Mode II fracture conditions, especially for joints with short initial crack length. The current study may help researchers deepen the understanding of interface shear fracture and clarify some previous concepts on this fracture mode.

1. Introduction

Adhesive bonding technology is being used in a variety of modern industries, including the automotive, aerospace, maritime, construction, defense, etc. Many components and structures, from microchips to ships and large aircrafts are made of materials arranged in layers through adhesive bonding. However, current design approaches for predicting the fracture of adhesively-bonded materials are still somewhat empirical, and improving these approaches is a critical issue for furthering the engineering applications of this technology. The most commonly used approach for analyzing the fracture of adhesive joints is interfacial fracture mechanics. Before the physical macro-crack is formed, the two surfaces of the adherends are held together by traction within a cohesive zone. The interfacial stresses vary according to the relative displacement of the surfaces, and an interface cohesive law describes the activities in the cohesive zone in terms of the separation and the traction of the interface to be formed during the fracture process.

Previous studies have focused on the development of test methods and modeling schemes for the characterization of Mode I adhesive fracture toughness in structural adhesive joints. However, the Mode II, or in-plane interface shear fracture, loading mode is of particular importance for adhesive joints (Blackman et al., 2005). Mode II loading may be induced when a cracked adhesive joint or a layered composite is subjected to bending. The various experimental fracture mechanics approaches to Mode II usually utilize some form of test specimen which is subjected to applied bending loads in order to determine values of the Mode II toughness G_{IIC} (Carlsson et al., 1986).

To measure the Mode II interlaminar fracture toughness, Russell (1982) introduced the customary end notched flexure (ENF) test, a three-point bending test as illustrated in Fig. 1. The compliance in bending is measured at several positions of the crack front with respect to the loading pin, and the load for the crack growth is determined for one definite crack position. The critical interlaminar fracture toughness is computed using the linear elastic fracture mechanics (LEFM) combined with data reduction techniques. The LEFM based measurement of Mode II toughness G_{IIc} showed that the critical load is sensitive to the crack length and delamination front profile in previous experimental studies (Bachrach et al., 1991; Schuecker and Davidson, 2000). Therefore, one test of the critical load may not be truly representative of a consistent G_{IIc}, and a number of tests are required.

However, this LEFM based approach relies on the existence of a crack in the interface, and on assumptions of small-scale bridging and linear-elasticity. If any of these conditions are violated, an

* Corresponding author. Address: Department of Mechanical Engineering, Louisiana State University, Baton Rouge, LA 70803, USA. Tel.: +1 225 578 5302; fax: +1 225 578 5924.
E-mail address: guoli@me.lsu.edu (G. Li).

0020-7683/$ - see front matter © 2009 Elsevier Ltd. All rights reserved.
doi:10.1016/j.ijsolstr.2009.02.011

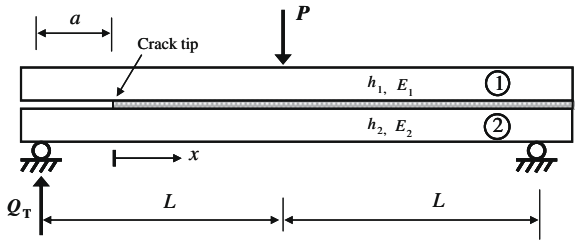

Fig. 1. The end notched flexure (ENF) specimen.

alternative approach such as cohesive-zone modeling is required (Needleman, 1987; Tvergaard and Hutchinson, 1992). As an alternative approach to the singularity driven fracture approach, the origins of the concept of cohesive zone model (CZM) goes back to the work of Barenblatt (1959) and Dugdale (1960). CZM has evolved as a preferred method to analyze fracture problems in monolithic and composite material systems not only because it avoids the singularity but also because it can be easily implemented in a numerical method of analysis such as in finite element modeling (Atkinson, 1979). Therefore, various CZMs have been proposed to investigate the fracture process in a number of material systems including fiber reinforced polymer composites, metallic materials, ceramic materials, cementitious or concrete materials, and bimaterial systems (Hillerborg et al., 1976; Rose et al., 1983; Needleman, 1987, 1990; Tvergaard, 1990; Tvergaard and Hutchinson, 1992; Xu and Needleman, 1993; Kinloch et al., 1994; Camacho and Ortiz, 1996; Geubelle and Baylor, 1998; Hutchinson and Evans, 2000; Williams and Hadavinia, 2002; Ouyang and Li, in press; Ouyang and Li, 2009).

One of the main problems that have been encountered with Mode II loading has been the poor reproducibility of the values of the measured Mode II toughness G_{IIC} (Davies et al., 1999). The effects of friction in the specimen could be a possible reason for this poor reproducibility. However, the experimental loading-unloading cycling test conducted by Russel and Street (1982) indicated a maximum error of around 2% in G_{IIC} in composites if friction was ignored. More recently, Davidson and Sun (2005) and Davidson et al. (2007) considered the effects of friction in the ENF specimen and 4-ENF tests were conducted on composites. They concluded that friction accounted for only about 2% and 5%, respectively, of the measured values of G_{IIC} from their tests.

Another possible major cause of scatter and inconsistency in Mode II toughness may be a difficulty in determining the location of the crack tip according to some recent studies (Schuecker and Davidson, 2000; Brunner, 2000; Brunner et al., 2006). The difficulty in determining the true crack length has also been observed during Mode I peel tests in composites when extensive fiber-bridging and microcracking occurs. This has been shown to cause variations and errors in the calculation of toughness when corrected beam theory was employed (Brunner, 2000). However, as an analytical model, the current study will focus on the critical load and its corresponding Mode II toughness at different initial precrack lengths, which can be clearly defined and well controlled in the actual tests. Therefore, the identification of crack length is not a concern in the current study.

Compared to the extensive studies and the well understanding of the Mode I interface fracture, further investigation on the Mode II interface shear fracture is needed. It seems that the complex damage mechanisms occurring around the crack tip and the lack of a universally agreed understanding of the interface shear fracture have all been suggested as the primary cause of the problem of poor reproducibility. The primary purpose of the current work is to develop a cohesive zone model (CZM) based analytical model for the interface shear fracture of end notched flexure (ENF) specimens. With this model, the scatter and inconsistency in Mode II toughness may be significantly reduced. And the strong dependency of the Mode II fracture toughness on the initial crack length as reported by the previous study (Bachrach et al., 1991) may be explained in a new perspective. Some important issues will be highlighted for the modeling and design of pure interface shear fracture. In addition, the distinct properties of Mode II shear fracture will also be discussed as compared to those of Mode I peel interface fracture.

2. Theoretical background

It is assumed that the crack separates in a monotonic fashion; neither unloading nor crack closure is permitted. The cohesive (or bridging) laws are assumed to be the same for each point along the bond length. Since the cohesive stresses represent the failure process zone, it may be also reasonable to assume that a certain crack opening exists, at which the cohesive stresses vanish when the failure criterion is satisfied. For the sake of simplicity, the classical beam theory is adopted in the current study.

An end notch adhesively bonded joint with a unit width is considered as shown in Fig. 1. In the end notch flexure specimen, the adhesive layer is assumed to be very thin and soft relative to the adherends. It is also assumed that the entire bond length $2L$ and L-a, which is the distance between the crack tip and the concentrated loading in mid-span are long enough. It is noted that the present analytical model is derived based on the configuration of adhesively bonded ENF joints with two adherends made of isotropic or orthotropic materials (identical or dissimilar materials). However, it may also be applicable to the ENF specimen with end notch or inserted crack starter foil if the cohesive zone is limited to the crack tip region and no large scale plasticity is developed in the upper and lower substrates.

It is also assumed that the nonlinear behavior of the entire adhesive layer under shear loadings can be well described by a nonlinear cohesive law. Since the nonlinear fracture behavior of the entire thin adhesive layer is normally dependent on the type and thickness of the adhesive layer, the thickness of the adhesive layer is not directly considered in the current work. Instead, an interface constitutive relationship (as described by the cohesive law) is assumed to be known once the adhesive type and thickness are given. In another word, the effect of the adhesive layer thickness is indirectly considered by the interface cohesive law.

Consider an infinitesimal section of the ENF specimen as shown in Fig. 2. Obviously, the relative tangential displacement δ between the bottom fiber of the upper adherend and the top fiber of the

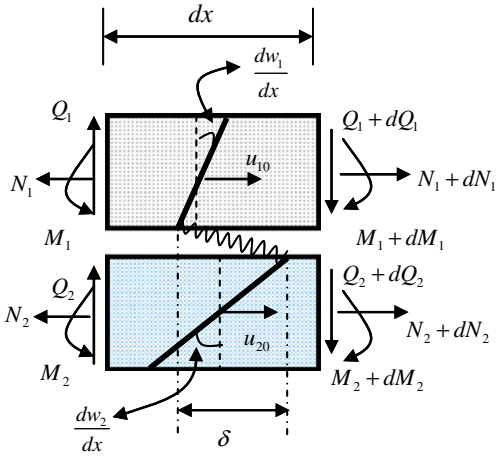

Fig. 2. Infinitesimal section of the end notched flexure (ENF) specimen.

lower adherend is contributed by two parts: (1) the longitudinal displacement of the neutral axis of each beam; and (2) the local rotation of each beam. Accordingly, the displacement field of the two beams (adherends) has the form

$$u_1(x_1,z_1)=u_{10}(x)+z_1\frac{dw_1(x)}{dx};\quad u_2(x,z_2)=u_{20}(x)+z_2\frac{dw_2(x)}{dx}$$
$$w_1(x,z_1)=w_1(x);\quad w_2(x,z_2)=w_2(x) \tag{1}$$

where $u_{10}(x)$ and $u_{20}(x)$ are displacements of the neutral plane of beams 1 and 2, respectively.

The longitudinal displacement of the bottom fiber of the upper beam u_1 and that of the top fiber of the bottom beam u_2 can be described as follows, respectively,

$$u_1=u_{10}-\frac{h_1}{2}\frac{dw_1(x)}{dx};\quad u_2=u_{20}+\frac{h_2}{2}\frac{dw_2(x)}{dx} \tag{2}$$

With Eq. (2), the relative interface displacement w (normal opening) between the bottom fiber of the upper adherend and the top fiber of the lower adherend can be expressed by

$$w=w_1-w_2;\quad \frac{dw}{dx}=\frac{dw_1}{dx}-\frac{dw_2}{dx} \tag{3}$$

According to Eq. (2), the relative tangential sliding δ (interface cohesive slip) between the upper adherend and lower adherend as illustrated by Fig. 2 can be expressed by

$$\delta=u_1-u_2=(u_{10}-u_{20})-\left(\frac{h_1}{2}\frac{dw_1}{dx}+\frac{h_2}{2}\frac{dw_2}{dx}\right) \tag{4}$$

The constitutive equations are written by

$$N_i=A_i\frac{du_{i0}}{dx};\quad M_i=D_i\frac{d^2w_i}{dx^2} \tag{5}$$

in which

$$A_i=\frac{E_{xi}h_i}{1-\nu_{xzi}\nu_{zxi}};\quad D_i=\frac{E_{xi}h_i^3}{12(1-\nu_{xzi}\nu_{zxi})}$$

The subscript $i=1,2$ represents the beams 1 and 2, respectively; N_i and M_i are the axial force and bending moment *per unit width* of the beam i ($i=1,2$) as illustrated in Fig. 1, respectively; A_i and D_i are the axial and bending stiffness of the beam i($i=1,2$) *per unit width* under the plane strain condition.

The equilibrium equations of each beam in the bonded region are written in the conventional way as

$$\frac{dN_1}{dx}=\tau(x);\quad \frac{dN_2}{dx}=-\tau(x);\quad \frac{dQ_1}{dx}=\sigma(x);\quad \frac{dQ_2}{dx}=-\sigma(x) \tag{6}$$
$$\frac{dM_1}{dx}=Q_1-\frac{h_1}{2}\tau(x);\quad \frac{dM_2}{dx}=Q_2-\frac{h_2}{2}\tau(x) \tag{7}$$
$$N_1+N_1=N_T;\quad Q_1+Q_2=Q_T;\quad M_1+M_2=M_T \tag{8}$$

With Eq. (4), it can be seen that

$$\delta'=-\frac{h_1}{2D_1}M_1+\frac{N_1}{A_1}-\left(\frac{h_2}{2D_2}M_2+\frac{N_2}{A_2}\right) \tag{9}$$

It is noted that the normal interface separation $w=w_1-w_2$, we thus have

$$w''=w_1''-w_2''=\left(\frac{M_1}{D_1}-\frac{M_2}{D_2}\right);$$
$$w'''=w_1'''-w_2'''=\left(\frac{1}{D_1}\frac{dM_1}{dx}-\frac{1}{D_2}\frac{dM_2}{dx}\right) \tag{10}$$

As illustrated by Fig. 1, when a joint is subjected to a transverse shear force Q_1 and Q_2 at the ends of the upper and lower substrate, respectively, there are bending moments $M_1=a\cdot Q_1$ and $M_2=a\cdot Q_2$ on the corresponding substrates at the location of the crack tip. With Eqs. (3)–(10), after lengthy derivations, the following equation can be derived

$$\delta''+\frac{h_1D_2-h_2D_1}{2(D_1+D_2)}w'''+\frac{h_1+h_2}{2(D_1+D_2)}Q_T=\left[\left(\frac{1}{A_1}+\frac{1}{A_2}\right)+\frac{(h_1+h_2)^2}{4(D_1+D_2)}\right]\tau \tag{11}$$

It is noted that $Q_1(x)+Q_2(x)=Q_T$, which is a constant along the longitudinal direction of the joint. This equation must be satisfied for a composite joint consisting of two beams with arbitrary geometry and material configurations if the classical beam theory is applied.

However, when $h_1D_2=h_2D_1$, the normal and tangential components can be completely decoupled. Eq. (11) can thus be reduced to the governing equation of a pure Mode II equation

$$\delta''+\frac{h_1+h_2}{2(D_1+D_2)}Q_T=\left[\left(\frac{1}{A_1}+\frac{1}{A_2}\right)+\frac{(h_1+h_2)^2}{4(D_1+D_2)}\right]\tau \tag{12}$$

Note the decoupling condition is given as follows:

$$h_1/D_1=h_2/D_2 \tag{13}$$

If the Poisson's ratio of the two adherends is identical or very close, Eq. (13) can be equivalent to the equation as follows:

$$h_2/h_1=\sqrt{E_1/E_2} \tag{14}$$

It is interesting to note that this decoupling condition does not require two identical beams. In another word, for the joints bonded with adherends made of dissimilar materials, Eq. (12) is still applicable if Eq. (13) is satisfied. The decoupled governing equation can significantly simplify the *J*-integral based analytical form of the interface fracture problems. As an effort on the analytical modeling, only the specimens which satisfy the decoupling condition are discussed in this study. Future work may be directed towards the conditions that Eq. (13) is not satisfied. However, this is beyond the scope of the current study.

3. Interface cohesive sliding behavior

With the decoupling condition that $h_1/D_1=h_2/D_2$ (note that it does not require $h_1=h_2$ and $E_1=E_2$ for the two substrates), the decoupled governing equation of the tangential interface shear behavior can be described by

$$\delta''+\frac{h_1+h_2}{2(D_1+D_2)}Q_T=\left[\frac{1}{A_1}+\frac{1}{A_2}+\frac{(h_1+h_2)^2}{4(D_1+D_2)}\right]\tau \tag{15}$$

An arbitrary shear cohesive law $\tau=\tau(\delta)$ is considered for the governing Eq. (15). Note that $Q_1+Q_2=Q_T$ ($Q_T=P/2$) is a constant along the x coordinate. Under the configuration in Fig. 1, the interface tangential sliding $\delta(x)$ must be a monotonic function of the coordinate x, although the interface shear stress $\tau(x)$ may be varied in a wave manner along the x direction due to the nonlinear relationship between δ and τ. The value of δ must be the highest positive at one end, and be the lowest negative at the other end under a given resultant transverse force Q_T as illustrated by Fig. 3. Obviously, there must be a zero-sliding point (δ_m is used to denote the slip at this point, and $\delta_m=0$) somewhere in the middle of the bonded length. Instead of solving the differential Eq. (15), let's consider an equivalent integral form as shown below,

$$\int\delta''d\delta+\frac{h_1+h_2}{2(D_1+D_2)}\int Q_Td\delta=\left[\left(\frac{1}{A_1}+\frac{1}{A_2}\right)+\frac{(h_1+h_2)^2}{4(D_1+D_2)}\right]\int\tau(\delta)d\delta \tag{16}$$

It can be observed that Eq. (16) is completely equivalent to Eq. (15). In other words, Eq. (15) is the equivalent differential form of the integral Eq. (16). However, it should be noted that such

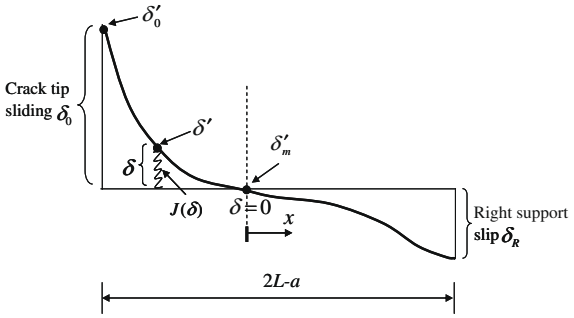

Fig. 3. The schematic of the distribution of relative interface slip δ and δ' along the bonded length.

equivalent integral form requires that each δ corresponds to a single value of the coordinate x, or this correspondence exists piecewisely along the bond length. Note that the change of x or δ along the longitudinal direction does not affect the value of Q_T, which is a constant along the x direction. Therefore, Eq. (16) can be rewritten by

$$\int\left(\frac{\partial\delta'}{\partial\delta}\delta'\right)d\delta+\frac{(h_1+h_2)Q_T}{2(D_1+D_2)}\int d\delta = \left[\left(\frac{1}{A_1}+\frac{1}{A_2}\right)+\frac{(h_1+h_2)^2}{4(D_1+D_2)}\right]\int\tau(\delta)d\delta \tag{17}$$

By integrating the interface slip δ from 0 to δ, it can be derived that,

$$\frac{1}{2}[(\delta')^2-(\delta_m')^2]+\frac{(h_1+h_2)Q_T}{2(D_1+D_2)}\delta = \left[\frac{1}{A_1}+\frac{1}{A_2}+\frac{(h_1+h_2)^2}{4(D_1+D_2)}\right]\cdot\int_0^{\delta}\tau(\delta)d\delta \tag{18}$$

where δ_m' is used to represent the derivative of δ at the zero slip point ($\delta_m = 0$).

It is important to notice that the integral limits on both sides of Eq. (17) must be correspondent to each other. Obviously, $\delta_m' \leftrightarrow \delta_m = 0$ (zero slip point) and $\delta' \leftrightarrow \delta$. It is also noted that $\delta_m' \neq 0$ unless $L\text{-}a \to \infty$. However, $\delta_m' \to 0$ or can be ignored when $L\text{-}a$ is long enough as seen in Fig. 3. Therefore, for the specimens with sufficiently long entire bond length and $L\text{-}a$, by denoting the tangential cohesive slip at the crack tip by δ_0, Eq. (18) can be simplified to,

$$\frac{1}{2}(\delta_0')^2+\frac{(h_1+h_2)Q_T}{2(D_1+D_2)}\delta_0=\left[\frac{1}{A_1}+\frac{1}{A_2}+\frac{(h_1+h_2)^2}{4(D_1+D_2)}\right]\cdot\int_0^{\delta_0}\tau(\delta)d\delta \tag{19}$$

Note that $Q_T = Q_1 + Q_2$ and $M_1 = a\cdot Q_1$ and $M_2 = a\cdot Q_2$, $N_1 = N_2 = 0$ at the ends. Associated with Eq. (9), the value of δ_0' can be readily expressed as a function of the transverse shear forces Q_1 and Q_2. Consequently, the Mode II energy release rate J_{II} can be written by

$$J_{II}(\delta_0)=\int_0^{\delta_0}\tau(\delta)d\delta = \frac{\frac{1}{2}\left[\frac{h_1a}{2D_1}Q_1+\frac{h_2a}{2D_2}Q_2\right]^2+\frac{(h_1+h_2)(Q_1+Q_2)}{2(D_1+D_2)}\delta_0}{\frac{1}{A_1}+\frac{1}{A_2}+\frac{(h_1+h_2)^2}{4(D_1+D_2)}} \tag{20}$$

Replacing $Q_1 + Q_2$ by the resultant shear force Q_T, and noticing that $h_1/D_1 = h_2/D_2$, the compact form of J_{II} is written by,

$$J_{II}(\delta_0)=\frac{\frac{1}{2}\left[\frac{h_1a}{2D_1}Q_T\right]^2+\frac{(h_1+h_2)Q_T}{2(D_1+D_2)}\delta_0}{\frac{1}{A_1}+\frac{1}{A_2}+\frac{(h_1+h_2)^2}{4(D_1+D_2)}} \tag{21}$$

Obviously, $Q_T = P/2$ as illustrated by Fig. 1. It can also be observed that Eq. (21) is indeed a quadratic equation of Q_T. By solving the quadratic equation, the positive root of Q_T is derived as the explicit function of the crack tip cohesive sliding δ_0 as follows:

$$Q_T=f(\delta_0)=\frac{\sqrt{X_2^2+4X_1X_3}-X_2}{2X_1} \tag{22}$$

where

$$X_1=\frac{1}{2}\cdot\left(\frac{h_1a}{2D_1}\right)^2;\quad X_2=\frac{(h_1+h_2)}{2(D_1+D_2)}\cdot\delta_0 \qquad X_3=\left[\frac{1}{A_1}+\frac{1}{A_2}+\frac{(h_1+h_2)^2}{4(D_1+D_2)}\right]\cdot\int_0^{\delta_0}\tau(\delta)d\delta \tag{23}$$

It is noted that the expression of Q_T shown in Eq. (22) is always positive since the term $X_1\cdot X_3$ is always positive unless $X_1 = 0$. When $X_1 = 0$, which can happen only when the initial crack length $a \to 0$, it implies that the first term on the left hand side of Eq. (19) is zero. With the reduced Eq. (19) (when $a \to 0$), Eq. (22) can be further reduced to

$$Q_T=\frac{\left[\frac{1}{A_1}+\frac{1}{A_2}+\frac{(h_1+h_2)^2}{4(D_1+D_2)}\right]\cdot\int_0^{\delta_0}\tau(\delta)d\delta}{\frac{(h_1+h_2)}{2(D_1+D_2)}\cdot\delta_0} \tag{24}$$

Eq. (22) explicitly correlates the crack tip cohesive sliding δ_0 to the resultant external force Q_T acting at the end of the ENF specimen if the overlap length is long enough. This means that the full crack initiation process under pure Mode II loading conditions can be simply described by a single function as shown in Eqs. (22) and (24). In order to predict the critical load P_{cr} (the maximum load capacity), a failure criterion is usually required. However, the current model for predicting the critical load of ENF specimen under pure Mode II loading does not have to specify a criterion, because with a properly defined interface cohesive law, the full Q_T-δ_0 curve can be obtained through Eq. (22), and the critical load can be identified.

It is important to note that the maximum load capacity normally does not correspond to the final crack tip cohesive sliding δ_f. We introduce a characteristic crack tip cohesive sliding δ_C, at which the load capacity Q_T reaches its maximum. The value of δ_C can be determined by Eq. (25) as follows:

$$\frac{dQ_T}{d\delta_0}=\frac{d\left[\frac{\sqrt{X_2^2+4X_1X_3}-X_2}{2X_1}\right]}{d\delta_0}=0 \tag{25}$$

With Eq. (23), after simplification, Eq. (25) can be rewritten by

$$\frac{K_1K_3}{K_2^2}\tau^2(\delta_C)+\delta_C\tau(\delta_C)=\int_0^{\delta_C}\tau(\delta)d\delta \tag{26}$$

where

$$K_1=\frac{1}{2}\cdot\left(\frac{h_1a}{2D_1}\right)^2;\quad K_2=\frac{(h_1+h_2)}{2(D_1+D_2)};\quad K_3=\left[\frac{1}{A_1}+\frac{1}{A_2}+\frac{(h_1+h_2)^2}{4(D_1+D_2)}\right] \tag{27}$$

If a standard end notched flexure (ENF) specimen (the adherends have identical thickness and are made of the same material) is considered, denoting $E_1 = E_2 = E$, $h_1 = h_2 = h$, $D_1 = D_2 = D$, Eq. (26) can be further simplified as follows:

$$\frac{4a^2}{Eh}\tau^2(\delta_C)+\delta_C\tau(\delta_C)=\int_0^{\delta_C}\tau(\delta)d\delta \tag{28}$$

When $a \to 0$, both Eqs. (26) and (28) can be further reduced to,

$$\delta_C\tau(\delta_C)=\int_0^{\delta_C}\tau(\delta)d\delta \tag{29}$$

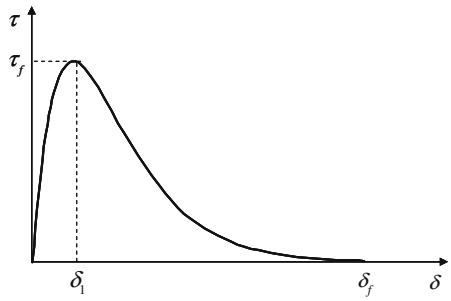

Fig. 4. A typical nonlinear interface cohesive law.

Eq. (29) indicates that when the crack length $a \to 0$, the value of the characteristic sliding δ_C is only dependent on the interface cohesive law; it is independent of the geometry and material property of the adherends.

It is also important to note that the characteristic sliding δ_C not necessarily exists for all cohesive laws. For a monotonically increasing cohesive law, the characteristic sliding δ_C does not exist since the integral (the area under the cohesive law curve) is always less than the product of τ and δ. This means the critical load (maximum load capacity) will not be achieved until the final separation δ_f (macro-debonding) is reached.

However, most real interface cohesive behaviors are governed by the ascending-descending types of cohesive laws as seen in Fig. 4. Therefore, the critical load is usually reached before the final separation δ_f. Comparing Eqs. (26) and (28) with Eq. (29), one can see that it is likely that the critical load is achieved at the characteristic sliding δ_C before the final separation δ_f due to the contribution of the first term in Eqs. (26) and (28).

On the other hand, by taking the derivative of both sides in Eq. (21) with respect to δ_0, together with the relationship between the energy release rate and the interface shear stress, the tangential cohesive shear stress τ can thus be determined as follows:

$$\frac{dJ_{II}(\delta_0)}{d\delta_0} = \tau(\delta_0) = \frac{\left[\left(\frac{h_1 a}{2D_1}\right)^2 Q_T + \frac{(h_1+h_2)}{2(D_1+D_2)}\delta_0\right]\frac{dQ_T}{d\delta_0} + \frac{(h_1+h_2)Q_T}{2(D_1+D_2)}}{\frac{1}{A_1}+\frac{1}{A_2}+\frac{(h_1+h_2)^2}{4(D_1+D_2)}} \tag{30}$$

Considering a typical ascending-descending type of cohesive law, we assume that the characteristic sliding δ_C exists. With the corresponding characteristic shear stress $\tau(\delta_C)$ as determined by Eq. (25), by inserting Eq. (26) into Eq. (24), the maximum load capacity $Q_{T\max}$ can be derived as follows:

$$Q_{T\max} = \frac{2(D_1+D_2)}{(h_1+h_2)}\left[\frac{1}{A_1}+\frac{1}{A_2}+\frac{(h_1+h_2)^2}{4(D_1+D_2)}\right]\cdot\tau(\delta_C) \tag{31}$$

For a standard end notched flexure (ENF) specimen with identical adherends, the maximum load capacity $Q_{T\max}$ can be further simplified to

$$Q_{T\max} = \frac{4}{3}h\cdot\tau(\delta_C) \tag{32}$$

Note that the characteristic sliding δ_C in Eqs. (31) and (32) can be obtained by Eq. (26). It is also noted that Q_T and $Q_{T\max}$ are the vertical forces per unit width. With Eqs. (31) and (32), one can see that the maximum load capacity $Q_{T\max}$ is proportional to the interface shear stress at the characteristic sliding δ_C. Eqs. (31) and (32) also indicate that the maximum interface shear stress has a significant effect on the critical load capacity $Q_{T\max}$. For the joint with very high Mode II toughness, while with relatively low interface shear strength, the load capacity of the ENF specimen is still limited as implied by Eqs. (31) and (32).

4. Validations and parametric studies

4.1. Experimental verifications

In order to verify the present model, a comprehensive comparison with the test results reported by Bachrach et al. (1991) is conducted. However, the detailed cohesive laws are not available for the specimens in their experiment. In order to calibrate the cohesive law according to their experimental data, a typical nonlinear law: exponential type of cohesive law is employed. This exponential law is described as follows:

$$\tau(\delta) = e\cdot\tau_f\frac{\delta}{\delta_1}\exp[-(\delta/\delta_1)] = (e\cdot\tau_f)^2\frac{\delta}{G_{IIC}}\exp\left[-\left(\frac{\delta}{G_{IIC}}\cdot e\tau_f\right)\right] \tag{33}$$

where τ_f is the interface shear strength (maximum shear stress), δ_1 is the cohesive sliding at which the interface shear stress τ reaches its maximum as seen in Fig. 4.

The current exponential type of cohesive law is a two-parameter model. With the given interface shear strength τ_f, the law is determined by adjusting the value of G_{IIc} until the experimental critical load is matched by Eq. (31). A typical interface shear strength $\tau_f = 25$ MPa is assumed. And the Mode II toughness G_{IIc} is calibrated to be 0.64 kJ/m^2. Note that only one set of test data (specimen A5 in Table 1) is used to calibrate the cohesive law. The calibrated cohesive zone model is then used to calculate the critical loads of all the remaining specimens. There are 28 test results with the predicted critical loads as listed in Table 1. The width b and total span length $2L$ of all the ENF specimens in their test (Bachrach et al., 1991) were 25.4 mm and 101.6 mm, respectively. A typical Poisson's ratio $\upsilon = 0.39$ of the carbon fiber reinforced composite laminate is assumed in the current study. The AS4/3501-6 graphite/epoxy unidirectional composite laminate was used for the specimens (32 plies in total) in their test. The initial crack was created by inserting Teflon between the two center plies. More details can be found in their original experimental study. The experimental and analytical results of the critical load are also plotted as a function of the initial crack length in Fig. 5. As pointed out by Bachrach et al. (1991), the experimental results are always difficult to compare for composite materials because of the different manufacturing processes and ply layups. From Table 1 and Fig. 5, one can see that the present prediction of the critical load agrees very well with the experimental data, and the total average error is less than 1%.

On the other hand, with the linear elastic fracture mechanics (LEFM) based model and the identical experimental data, Bachrach et al. (1991) calculated the values of Mode II toughness G_{IIc} as a function of the initial crack length a_0. They found that the Mode II toughness G_{IIc} was strongly dependent on the initial crack length a_0. According to their model (Bachrach et al., 1991), the value of G_{IIc} increased by approximately 50% when the initial crack length a_0 was increased from 0.4 L to 0.8 L (L = 50.8 mm). If a larger variation range of the initial crack length is considered, such as the initial crack length is varied from zero to 0.8 L, it is expected that the variation in G_{IIc} with the change of the initial crack length should be more significant with their model.

However, with the same experimental data, the current model presents a distinctly different conclusion. The current results indicate that the Mode II toughness G_{IIc} under pure Mode II shear cracking is indeed independent of or very weakly dependent on the initial crack length a_0. This conclusion is well supported by the good agreement with their experimental results as listed in Table 1 and shown in Fig. 5. It is important to note that only one test result of a single specimen is used to calibrate the interface cohesive law. However, with this calibrated cohesive law, the critical loads of the entire 28 specimens with completely different

Table 1
Comparison of experimental results (Bachrach et al., 1991) and the present analytical solution of the critical loads.

	Specimen Number	a (mm)	h (mm)	P_{cr} (test) (N)	Present (N)	Error (%)
Group A	A1	40.13	1.723	533.3	484.0	9.3
	A2	38.10	1.727	514.2	505.8	1.6
	A3	34.54	1.725	540.9	546.2	−1.0
	A4	30.99	1.734	582.7	595.2	−2.1
	A5	27.94	1.728	643.2	646.3	−0.5
	A6	26.42	1.721	654.3	671.2	−2.6
	A7	24.89	1.715	699.7	703.3	−0.5
Group B	B1	39.12	1.977	643.2	596.9	7.2
	B2	35.56	1.989	654.3	652.1	0.3
	B3	31.50	1.995	688.6	718.8	−4.4
	B4	28.49	2.002	752.6	783.3	−4.1
	B5	25.40	2.009	839.8	857.6	−2.1
	B6	24.89	2.007	824.7	871.0	−5.6
	B7	21.84	2.005	949.2	959.9	−1.1
Group C	C1	40.64	2.137	684.6	646.3	5.6
	C2	37.59	2.149	703.7	701.0	0.4
	C3	34.54	2.173	749.1	755.7	−0.9
	C4	32.51	2.184	790.4	797.1	−0.8
	C5	29.97	2.193	798.0	849.2	−6.4
	C6	25.40	2.203	888.8	978.2	−10.1
	C7	24.89	2.209	979.5	988.4	−0.9
Group D	D1	38.61	2.139	699.7	684.6	2.2
	D2	36.58	2.145	711.3	710.4	0.1
	D3	34.04	2.160	752.6	762.9	−1.4
	D4	32.51	2.176	760.2	790.0	−3.9
	D5	28.96	2.183	839.8	872.3	−3.9
	D6	24.89	2.189	979.5	987.9	−0.9
	D7	22.86	2.182	1081.8	1052.9	2.7
Total average error						**−0.8**

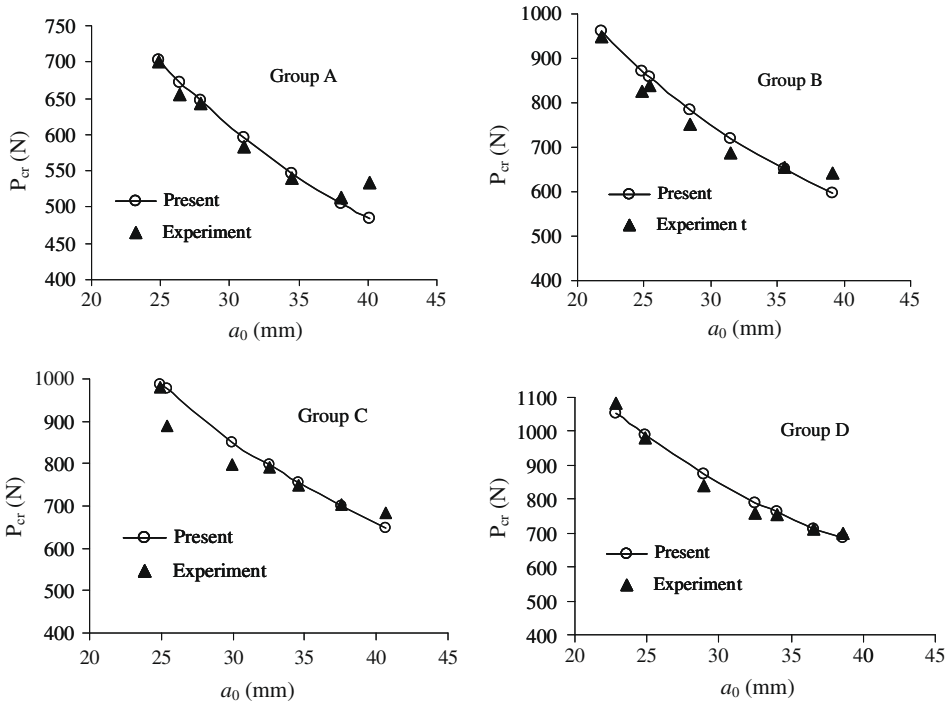

Fig. 5. Comparison of experimental results (Bachrach et al., 1991) and analytical results of the critical load P_{cr} at different crack length.

crack lengths are well predicted by the single identical cohesive zone model. If the calibration is conducted for each group (four groups in total), the prediction should be even better. Considering the possible constraint effect of geometry, the real cohesive behavior may be slightly affected. However, this variation due to different initial crack length is very limited, which is much lower than 50% as reported by Bachrach et al. (1991). In another word, for the given physical interface properties and adhesive layer thickness, the properly defined shear cohesive law seems relatively stable under pure Mode II conditions for different initial crack length. This phenomenon for the Mode II shear fracture seems different from the well accepted understanding of the interface fracture behavior of bonded joint under pure Mode I (peel loading) conditions (Blackman et al., 2003).

Fundamentally, the effect of the crack length and crack tip sliding δ_0 on the external load has been included in the present model as seen in Eq. (22). Therefore, it is not necessary to incorporate the crack length into the expression of Mode II toughness G_{IIc} due to its weak correlation to the crack length. The value of G_{IIc} can thus be treated in a certain sense as a material constant for the provided physical interface property and thickness of the adhesive layer. Consequently, the relaxation of the dependence of the cohesive law on the geometry may significantly facilitate the modeling of interface shear fracture. Based on the crack length dependent models in the previous studies, the calculated Mode II toughness values scattered very significantly. Also, the scattered value of G_{IIc} causes the difficulty in the accurate prediction of the critical loads for the interface shear fracture of ENF specimens. The present model may provide better prediction capabilities.

4.2. Parametric studies

With the verified model, a comprehensive parametric study is conducted in this section. The effect of the specimen's geometry and material property, the interface shear strength, the type of cohesive law and the Mode II toughness on critical loads is investigated. In all of the parametric studies, the identical interface cohesive law is assumed to be exponential type of model as described by Eq. (33), expect for the parametric study on the type of cohesive laws. For all cohesive laws, the interface shear strength τ_f = 25 MPa except for the parametric study on the interface shear strength. The Mode II toughness G_{IIc} is set as 0.64 kJ/m^2 except for the parametric study on Mode II toughness. The span and width of all ENF specimens are $2L$ = 200 mm and 1 mm, respectively, for all parametric studies. The Poisson's ratio of all adherends (identical or dissimilar adherends) are υ = 0.32. The elastic modulus and thickness of all adherends are 150 GPa and 4 mm, respectively, except for the parametric study on the geometry.

4.2.1. Effect of geometry and material properties

The critical load at crack length a = 0 is denoted by P_{cr0}. Note P_{cr0} is the highest critical load for the given configuration. The normalized critical loads P_{cr}/P_{cr0} for the specimen joined with identical adherends are plotted as a function of the initial crack length a_0 in Fig. 6. Note that for the specimens with identical adherends, $E_1 = E_2 = E$ = 150 GPa, $h_1 = h_2 = h$, as illustrated in Fig. 6, the critical load P_{cr0} (at crack length a = 0) is proportional to the thickness h. This phenomenon is valid for most ascending-descending types of nonlinear cohesive laws and can be explained by Eqs. (29) and (32) as discussed before. However, with the growth of crack length, the critical load P_{cr} is no longer proportional to the thickness of the adherend. It is interesting to find that thicker adherends not only lead to higher P_{cr} but also reduce the rate of decrease with the increase of the crack length.

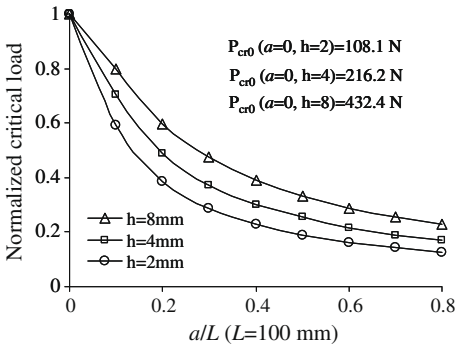

Fig. 6. Normalized critical load vs. crack length at different adherend's thickness h = 2, 4, 8 mm.

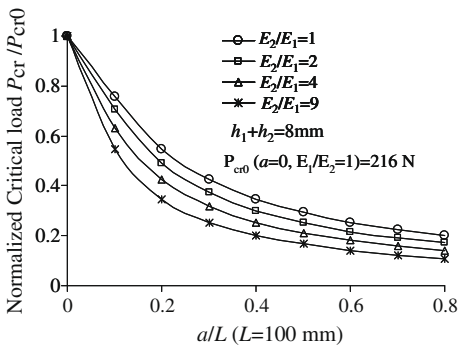

Fig. 7. Normalized critical load vs. crack length with different adherend's modulus ratio.

In order to investigate the shear fracture behavior of specimens bonded with two dissimilar adherends, a specimen with a total thickness of $h_1 + h_2$ = 8 mm is considered. In the specimen, E_2 = 220 GPa, and four different elastic modulus ratios E_2/E_1 are considered: E_2/E_1 = 9, 4, 2, and 1. According to the decoupling condition Eq. (14), the thickness ratio h_1/h_2 for the specimen can be calculated by the square root of E_2/E_1. By maintaining the total thickness of $h_1 + h_2$ = 8 mm, the individual thickness h_1 and h_2 can thus be determined. Fig. 7 plots the relationship between the normalized critical load P_{cr} and crack length with different modulus ratios. One can see that when the crack length approaches zero, the difference between the critical loads disappears. While at a relatively small crack length, such as a/L = 0.2 (L = 100 mm), the critical loads show the largest difference although the specimens have the identical total thickness. Fig. 7 also indicates that the identical adherend configuration (E_1/E_2 = 1) leads to the highest shear fracture resistance for all the different crack lengths considered. On the other hand, when the crack length a_0 is very small, by adjusting the modulus ratio, the bending stiffness can be conveniently increased while maintaining identical total thickness and shear fracture load capacity.

4.2.2. Effect of interface shear strength

With the identical Mode II toughness G_{IIc} = 0.64 kJ/m^2 and the same type of cohesive law (exponential type law), the effect of interface shear strength τ_f on the relationship between the crack tip sliding and external load is shown in Figs. 8a–c for different initial crack lengths. Four different interface shear strength τ_f = 2.5, 10, 25 and 40 MPa are investigated. As illustrated in Fig. 8, the interface shear strength has a dominant effect on the critical loads (the peak external loads in the P-δ_0 curves) when the initial crack length approaches zero. While in Fig. 8b and c, the interface shear strength still significantly affects the critical loads with medium or long crack length. It is noted that all the curves have the same Mode II toughness G_{IIc}. From Fig. 8, one can also see that the increase in crack length reduces the difference in the critical load caused by the different interface shear strength. The strong dependency of the critical load on the interface shear strength τ_f can be explained by Eq. (31) as discussed previously.

4.2.3. Effect of Mode II fracture toughness

With the same interface shear strength τ_f = 25 MPa and the same type of cohesive law (exponential type law), the effect of the Mode II toughness on the critical load is studied. Three Mode II toughnesses G_{IIc} = 0.32, 0.64 and 1.28 kJ/m^2 are studied. The critical load is plotted as a function of the initial crack length in Fig. 9 for different Mode II toughnesses. As shown in Fig. 9, the critical

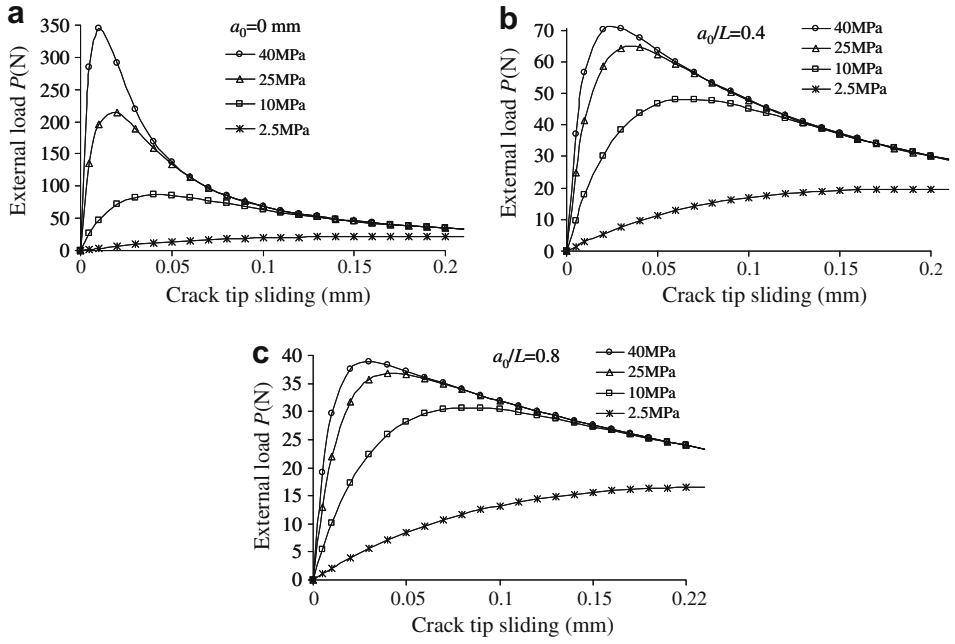

Fig. 8. (a) External load P vs. crack tip sliding at $a/L = 0$ ($L = 100$ mm) for different shear strength τ_f and $G_{IIC} = 0.64$ kJ/m^2. (b) External load P vs. crack tip sliding at $a/L = 0.4$ ($L = 100$ mm) for different shear strength τ_f and $G_{IIC} = 0.64$ kJ/m^2. (c) External load P vs. crack tip sliding at $a/L = 0.8$ ($L = 100$ mm) for different shear strength τ_f and $G_{IIC} = 0.64$ kJ/m^2.

load is identical when the crack length approaches zero, even with completely different Mode II toughness. The trend is exactly opposite to the trend in the effect of the interface shear strength on the critical load. Therefore, when the initial crack length is very short, higher critical fracture toughness indeed cannot increase the shear fracture load capacity. In order to improve the critical load, high interface shear strength should be applied if the initial crack length is very short. One can also see that the critical load decreases with the increase of the initial crack length. However, it is noted that the decrease rate with the initial crack length is different. As illustrated in Fig. 9, higher Mode II toughness decreases relatively slower.

4.2.4. Effect of the type of the cohesive law

With the identical interface shear strength $\tau_f = 25$ MPa and the same Mode II toughness $G_{IIc} = 0.64$ kJ/m^2, the effect of five different types of cohesive laws are investigated. They are equivalent linear elastic model, bilinear model, cubic model, equivalent constant stress model and exponential model, as shown in Fig. 10. The detailed expressions of these laws can be found in the Appendix. The relationships between the external load and the crack tip sliding are plotted in Fig. 11a–d for different initial crack lengths, respectively. One can see that when the initial crack length is relatively small (such as $a = 0$ or $a/L = 0.1$), the shape of the cohesive law has a significant effect on the P-δ curves as well as the critical load P_{cr}. This dependence of the critical load on the cohesive law is another important difference between Mode I peel fracture and Mode II shear fracture. Previous studies (Williams and Hadavinia, 2002; Blackman et al., 2003; Ouyang and Li, in press) indicated that the critical load of DCB specimens under pure Mode I condition is weakly dependent on the detailed shape of the cohesive law. With the same interface normal strength σ_f and Mode I toughness G_{Ic}, the variation of the critical load due to the change of the cohesive law can even be ignored. Evidently, this conclusion does not seem to be applicable to the Mode II interface shear fracture. However, this shape effect gradually decreases with the increase of the initial crack length. The critical loads predicted by different cohesive laws converge into the same value when a relatively long initial crack length ($a/L = 0.8$) is considered as illustrated by Fig. 11. One can also see from Fig. 11 that the equivalent linear elastic model yields the lowest prediction, while the equivalent constant stress model predicts the highest critical load. The other three typical nonlinear laws: bilinear, cubic and exponential offer relatively similar predictions among them. The three typical nonlinear

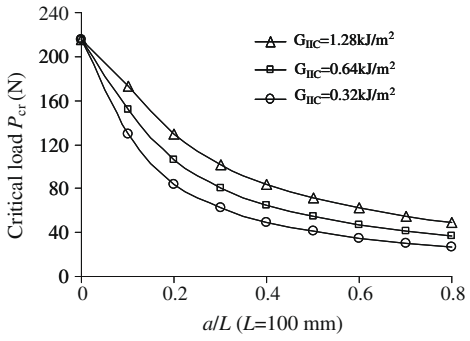

Fig. 9. Critical load P_{cr} vs. crack length with different Mode II toughness G_{IIc}.

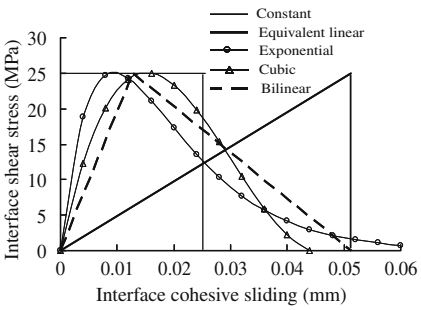

Fig. 10. Various interface cohesive laws with Mode II toughness $G_{IIc} = 0.64$ kJ/m^2 and $\tau_f = 25$ MPa.

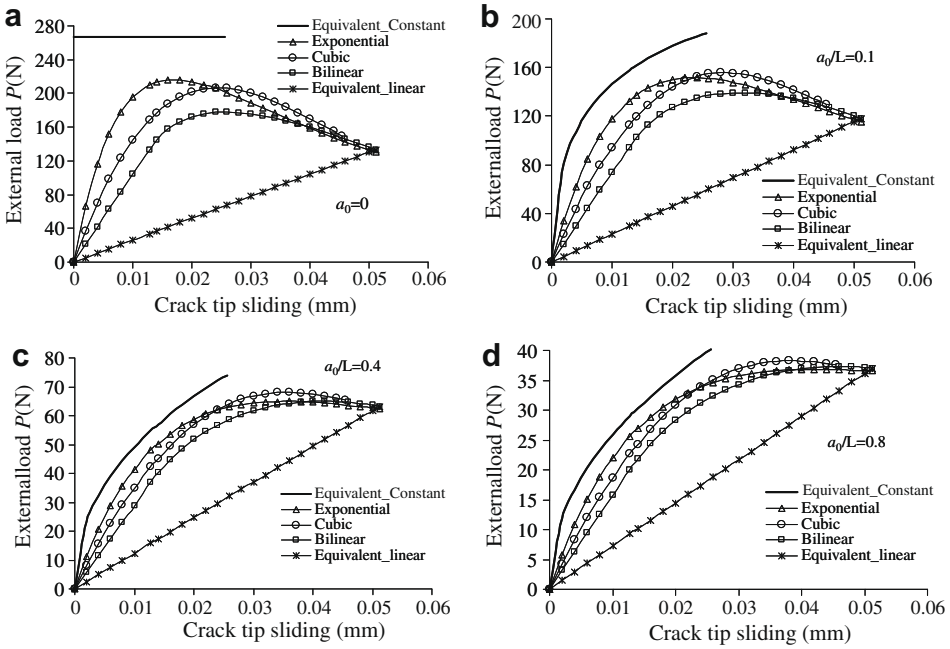

Fig. 11. (a) External load P vs. crack tip sliding with various interface cohesive laws at $a/L = 0$ ($L = 100$ mm). (b) External load P vs. crack tip sliding with various interface cohesive laws at $a/L = 0.1$ ($L = 100$ mm). (c) External load P vs. crack tip sliding with various interface cohesive laws at $a/L = 0.4$ ($L = 100$ mm). (d) External load P vs. crack tip sliding with various interface cohesive laws at $a/L = 0.8$ ($L = 100$ mm).

models may largely represent the real cohesive fracture behavior. This implies that when short or medium initial crack length is considered, the equivalent linear elastic model may be difficult to well simulate the interface shear fracture of ENF specimens.

5. Conclusions

In the current study, a cohesive zone model (CZM) based analytical modeling is developed for the interface shear fracture of end notched flexure (ENF) specimens. It is found that the scatter and inconsistency in Mode II toughness may be significantly reduced by this model. The current work indicates that for the given physical interface properties and adhesive layer thickness, the properly defined shear cohesive law seems relatively stable under pure Mode II conditions for different initial crack length; and this conclusion is well supported by the good agreement with the experimental results. By incorporating the crack length and external force and crack tip sliding into a compact formulation, the Mode II toughness G_{IIc} under pure shear cracking condition is indeed independent of or very weakly dependent on the initial crack length.

The comprehensive parametric studies show that the interface shear strength has the most dominant effect on the critical load, especially for relatively short initial crack length. It is also interesting to find that with very short initial crack length, higher Mode II toughness indeed cannot improve the critical load. Unlike the very weak dependence of the critical load on the detailed shape of the cohesive law for Mode I peel fracture, the shape of the cohesive law becomes relatively important for the critical load under pure interlaminar shear fracture conditions. The phenomenon seems especially significant when the initial crack length is short. The current study may help researchers deepen the understanding of interface shear fracture and clarify some previous concepts on this fracture mode.

Acknowledgement

This study is based upon work supported by the NSF under Grant No. (NSF 0734845) and by the NASA/EPSCoR under Grant No. NASA/LEQSF (2007-10)-Phase3-01.

Appendix A

Constant stress type of law:

$$\tau(\delta) = \begin{cases} \tau_f & 0 \le \delta < \delta_f \\ 0 & \delta \ge \delta_f \end{cases} \tag{A1}$$

Linear elastic type of law:

$$\tau(\delta) = \begin{cases} \frac{\tau_f^2}{2G_f}\delta & 0 \le \delta < \delta_f \\ 0 & \delta \ge \delta_f \end{cases} \tag{A2}$$

Bilinear type of law ($\delta_1 = \delta_f/4$):

$$\tau(\delta) = \begin{cases} 2\tau_f^2\delta/G_f & 0 \leqslant \delta \leqslant \delta_1 \\ 2\tau_f(2G_f - \delta\tau_f)/3G_f & \delta_1 \leqslant \delta \leqslant \delta_f \\ 0 & \delta_f \leqslant \delta \end{cases} \tag{A3}$$

Cubic type of law ($\delta_1 = \delta_f/3$):

$$\tau(\delta) = \frac{27}{4}\tau_f\frac{\delta}{\delta_f}\left(1 - \frac{\delta}{\delta_f}\right)^2 = \frac{243}{64}\frac{\tau_f^2}{G_f}\delta\left(1 - \frac{9}{16}\frac{\tau_f}{G_f}\delta\right)^2 \tag{A4}$$

Exponential type of law:

$$\begin{aligned}\tau(\delta) &= e\cdot\tau_f\frac{\delta}{\delta_1}\exp[-(\delta/\delta_1)] \\ &= (e\cdot\tau_f)^2\frac{\delta}{G_{IIC}}\exp\left[-\left(\frac{\delta}{G_{IIC}}\cdot e\tau_f\right)\right]\end{aligned} \tag{A5}$$

References

Atkinson, C., 1979. Stress singularities and fracture mechanics. Applied Mechanics Review 32 (2), 123–135.

Bachrach, W.E., Hicks, Th.R., Habas, Z.S., Granata, D.M., 1991. Mixed experimental–structural model for interlaminar shear fracture toughness. Journal of Aerospace Engineering 4 (1), 108–125.

Barenblatt, G.I., 1959. The formation of equilibrium cracks during brittle fracture. General ideas and hypothesis. Axisymmetrical cracks. Journal of Applied Mathematics and Mechanics (PMM) 23 (3), 622–636. English Translation.

Blackman, B.R.K., Hadavinia, H., Kinloch, A.J., Williams, J.G., 2003. The use of a cohesive zone model to study the fracture of fibre composites and adhesively-bonded joints. International Journal of Fracture 119, 25–46.

Blackman, B.R.K., Kinloch, A.J., Paraschi, M., 2005. The determination of the mode II adhesive fracture resistance, G_{IIC}, of structural adhesive joints: an effective crack length approach. Engineering Fracture Mechanics 72, 877–897.

Brunner, A.J., 2000. Experimental aspects of mode I and mode II fracture toughness testing of fibre-reinforced polymer–matrix composites. Computer Methods in Applied Mechanics and Engineering 185, 161–172.

Brunner, A.J., Blackman, B.R.K., Williams, J.G., 2006. Calculating a damage parameter and bridging stress from G_{IC} delamination tests on fibre composites. Composites Science and Technology 66, 785–795.

Camacho, G.T., Ortiz, M., 1996. Computational modeling of impact damage in brittle materials. International Journal of Solids and Structures 33, 2899–2938.

Carlsson, L.A., Gillespie, J.W., Pipes, R.B., 1986. On the analysis and design of the end notched flexure (ENF) specimen for mode II testing. Journal of Composite Materials 20, 594–604.

Davidson, B.D., Sun, X., 2005. Effects of friction, geometry and fixture compliance on the perceived toughness from three and four point bended notched flexure tests. Journal of Reinforced Plastic Composites 4 (15), 1611–1628.

Davidson, B.D., Sun, X., Vinciquerra, A., 2007. Influences of friction, geometric nonlinearities, and fixture compliance on experimentally observed toughnesses from three and four-point bend end-notched flexure tests. Journal of Composite Materials 41 (10), 1177–1196.

Davies, P., Sims, G.D., Blackman, B.R.K., Brunner, A.J., Kageyama, K., Hojo, M., Tanaka, K., Murri, G., Rousseau, C., Gieseke, B., Martin, R.H., 1999. Comparison of test configurations for determination of mode II interlaminar fracture toughness results from international collaborative test programme. Plastics Rubber Composite 28 (9), 432–437.

Dugdale, D.S., 1960. Yielding of steel sheets containing slits. Journal of the Mechanics and Physics of Solids 8, 100–104.

Geubelle, P.H., Baylor, J.S., 1998. The impact-induced delamination of laminated composites: a 2D simulation. Composites Part B: Engineering 29, 589–602.

Hillerborg, A., Modéer, M., Petersson, P.E., 1976. Analysis of crack formation and crack growth in concrete by means of fracture mechanics and finite elements. Cement and Concrete Research 6, 773–782.

Hutchinson, J.W., Evans, A.G., 2000. Mechanics of materials: top–down approaches to fracture. Acta Materialia 48, 125–135.

Kinloch, A.J., Lau, C.C., Williams, J.G., 1994. The peeling of flexible laminates. International Journal of Fracture 66, 45–70.

Needleman, A., 1987. A continuum model for void nucleation by inclusion debonding. ASME Journal of Applied Mechanics 54, 525–531.

Needleman, A., 1990. An analysis of tensile decohesion along an interface. Journal of the Mechanics and Physics of Solids 38, 289–324.

Ouyang, Z., Li, G., in press. Local damage evolution of DCB specimens during crack initiation process: a natural boundary condition based method. ASME Journal of Applied Mechanics.

Ouyang, Z., Li, G., 2009. Cohesive zone model based analytical solutions for adhesively bonded pipe joints under torsional loading. International Journal of Solids and Structures 46 (5), 1205–1217.

Rose, J.H., Smith, J.R., Ferrante, J., 1983. Universal features of bonding in metals. Physical Review B 28, 1835–1845.

Russell, A.J., Street, K.N. 1982. Factors affecting the interlaminar fracture energy of graphite/epoxy laminates. In: ICCM-IV, Tokyo, Japan, 1982.

Russell, A.J., 1982. On the measurement of mode II interlaminar fracture energies. Materials Report 82-0, Defence Research, Establishment Pacific, Victoria, British Columbia, Canada.

Schuecker, C., Davidson, B.D., 2000. Evaluation of the accuracy of the four-point bend end-notched flexure test for the mode II delamination toughness determination. Composite Science and Technology 60, 2137–2146.

Tvergaard, V., 1990. Effect of fibre debonding in a whisker-reinforced metal. Materials Science and Engineering A 125, 203–213.

Tvergaard, V., Hutchinson, J.W., 1992. The relation between crack growth resistance and fracture process parameters in elastic–plastic solids. Journal of the Mechanics and Physics of Solids 40, 1377–1397.

Williams, J.G., Hadavinia, H., 2002. Analytical solutions for cohesive zone models. Journal of the Mechanics and Physics of Solids 50, 809–825.

Xu, X.P., Needleman, A., 1993. Void nucleation by inclusion debonding in a crystal matrix. Modeling and Simulation in Materials Science and Engineering 1, 111–132.